

ABSTRACT

Title of dissertation: Measuring topology of BECs
in a synthetic dimensions lattice

Dina Genkina
Doctor of Philosophy, 2018

Dissertation directed by: Professor Ian Spielman
Department of Physics

Measuring topology of BECs in a synthetic dimensions lattice

by

Dina Genkina

Dissertation submitted to the Faculty of the Graduate School of the
University of Maryland, College Park in partial fulfillment
of the requirements for the degree of
Doctor of Philosophy
2018

Advisory Committee:
Professor Ian Spielman, Chair/Advisor

© Copyright by
Dina Genkina
2018

Chapter 2: Atom Light Interactions

2.1 Near-resonant atom-light interaction

In this section, we will assume the atom can be treated as a two-level system: one with a ground and excited atomic state, with an energy difference of energy difference $\hbar\omega_0$. When such an atom, starting in the ground state, is illuminated by a laser beam with frequency $\hbar\omega_L$, there are three kinds of transitions that occur: during absorption the atom absorbs a photon from the laser and goes from the ground to the excited state; during stimulated emission, the atom emits a photon into the field of the laser beam and jump from the excited to the ground state; during spontaneous emission, the atom decays to the ground state from the excited state with no help from the laser, emitting into a random vacuum mode. Stimulated emission results in coherent light co-propagating with the laser beam, while spontaneous emission results in light scattering incoherently in any direction. The rate of spontaneous emission from an excited state is given by the natural transition linewidth of the transition Γ .

On timescales short compared to $1/\Gamma$, spontaneous emission can be ignored, and an atom undergoes coherent Rabi oscillations between the ground and excited states via cycles of absorption and stimulated emission [1]. Taking c_g and c_e to be the time-dependent coefficients multiplying the eigenstate wavefunctions of the ground and excited state respectively, and assuming the atom starts in the ground

state $c_g(t = 0) = 1$, the excited state population is given by

$$c_e(t) = -i \frac{\Omega}{\Omega'} \sin\left(\frac{\Omega' t}{2}\right) e^{-i\delta t/2}, \quad (2.1)$$

where Ω is the Rabi frequency given by $\Omega^2 = \frac{\Gamma \lambda_L^3}{h(2\pi)^3} I$, with λ_L as the laser wavelength, h as Plank's constant and I as the laser intensity, $\Omega' = \sqrt{\Omega^2 + \delta^2}$ is the generalized Rabi frequency and $\delta = \omega_0 - \omega_L$ is the detuning of the laser from atomic resonance.

In the regime where spontaneous emission cannot be ignored, Rabi oscillations of each individual atom are intermittently interrupted by decay to the ground state. Averaging over an atomic ensemble, on the time scale of a single Rabi oscillation the overall excited state population reaches a steady state, and the rate of spontaneous emission becomes constant. Since during spontaneous emission the ejected photon can go into any vacuum mode, this process can be thought of as the scattering of photons by the atoms. This scattering rate is given by [1]

$$\gamma_{\text{sc}} = \frac{\Gamma}{2} \frac{I/I_{\text{sat}}}{1 + 4(\delta/\Gamma)^2 + I/I_{\text{sat}}}, \quad (2.2)$$

where I_{sat} is the saturation intensity. This is the intensity at which the timescale of spontaneous emission matches the Rabi oscillation rate, reducing the capacity for absorption of extra light.

2.2 Absorption imaging

Absorption imaging takes advantage of the on-resonant interaction described in the previous section. An on or near-resonant laser beam ($\delta/\Gamma \ll 1$) is shined at the atoms, and the absorbed light acts to create a shadow in the shape of the atoms in the laser beam. This beam with the shadow is then imaged on a camera, in our case a CCD, as depicted in Figure 1a (top). This is called the atom image,

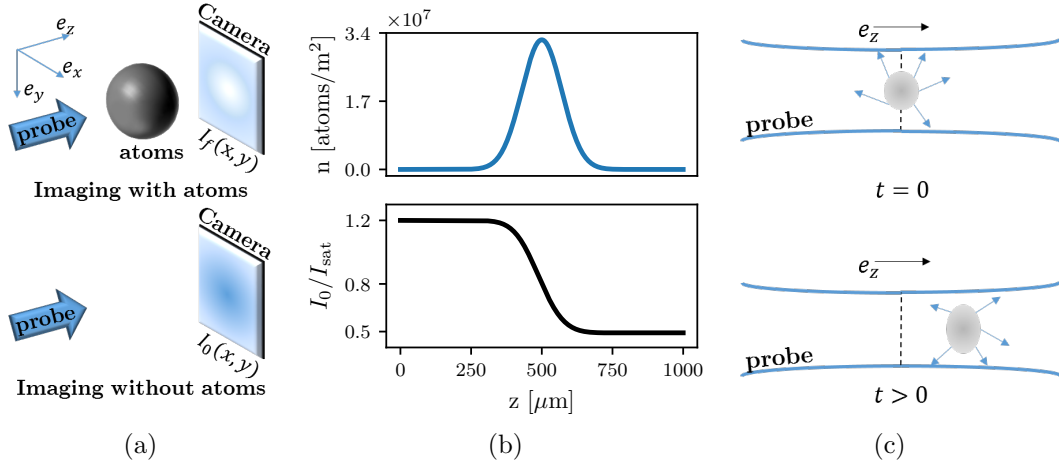


Figure 1: Absorption imaging. (a) Near resonant probe light illuminates the atoms, and the transmitted light (containing a shadow of the atoms) is imaged on the camera. A second image taken with no atoms provides a reference. (b) The probe beam is partially absorbed as it traverses the cloud, and the intensity seen by atoms further along the imaging direction e_z is lowered. (c) An atomic cloud illuminated by a probe light field absorbs photons from the probe and re-emits them in all directions. This process results in a net acceleration of the cloud in the direction of the probe light as well as diffusive spreading in the transverse directions.

and the intensity distribution over the camera is denoted by $I_f(x, y)$, where the subscript f stands for final - the intensity after the light has encountered the atoms. To quantify the 'shadowed out' intensity, after the atoms have left the trap the same laser intensity is shined directly at the camera, as in Figure 1a (bottom). This is called the probe image, and the intensity distribution over the camera is denoted by $I_0(x, y)$, where the subscript 0 indicated initial - the intensity before the light had encountered the atoms.

To recover the atom number distribution encountered by the light, consider an atomic cloud with 3D density $\rho(x, y, z)$. Since we can only obtain 2D information from the camera, we can only hope to recover a 2D atomic column density $n(x, y) = \int \rho(x, y, z) dz$. Focusing in on a single pixel of the camera, we can consider a single value of I_0 and I_f to recover a local n . As the laser light propagates through the atomic cloud, the intensity of the light will diminish due to absorption. This

absorption as a function of propagation direction z can be expressed using the scattering rate equation Eq. 2.2 as the number of photons scattered by the atoms (proportional to the atomic density times the scattering rate) times the photon energy $\hbar\omega_L$:

$$\frac{d}{dz} \frac{I(z)}{I_{\text{sat}}} = -\hbar\omega_L \rho(z) \gamma_{sc}(z) = -\rho(z) \sigma_0 \frac{I(z)/I_{\text{sat}}}{1 + 4\delta^2/\Gamma^2 + I(z)/I_{\text{sat}}}, \quad (2.3)$$

where the resonant scattering cross section is $\sigma_0 = 3\lambda_0^2/2\pi$, and λ_0 is the wavelength associated with atomic resonance.

Integrating both sides of Eq. 2.3, we obtain

$$\sigma_0 n = (1 + 4\delta^2/\Gamma^2) \ln(I_0/I_f) + (I_0 - I_f)/I_{\text{sat}}. \quad (2.4)$$

The quantity $OD = \ln(I_0/I_f)$ is called the optical depth of the cloud. When the probe intensity I_0 is much smaller than the saturation intensity, the second term in Eq. 2.4 becomes negligible. Assuming further that the probe light is on resonance, $\delta = 0$, the atomic column density becomes simply $\sigma_0 n = OD$. Figure 1b shows a Gaussian atomic density distribution (top) and the resulting probe intensity as a function of position in the cloud (bottom). The intensity drops from its initial to final value gradually as it traverses the cloud.

However, there is an important effect that the above equations do not account for. Namely, as the atoms absorb light from the probe beam, they also get a momentum kick equal to the momentum of a photon during each collision $\hbar k_r = h/\lambda_L$ in the direction of propagation. It is true that the absorbed photon will then be re-emitted by the atom, inducing a loss of momentum, but since this happens through the process of spontaneous emission into a random vacuum mode, the average momentum kick acquired this way over many re-emissions will average to zero. On average, each photon absorbed will induce a change in velocity of the atom of $v_r = \hbar k_r/m$,

where m is the atomic mass, as depicted in Fig. 1c. As the velocity of the atom changes, due to the Doppler effect, the apparent laser frequency will change as well. Therefore, even if the laser light is exactly on-resonant for a stationary atom, it will become off-resonant for longer imaging times, and Eq. 2.3 will acquire a time dependence. For most experiments, this effect is small and can be neglected. However, if the imaging time becomes of order a recoil time t_r , a time after which the recoil-induced detuning δ becomes of order Γ , this effect becomes significant. We explore this effect in Chapter ??.

2.3 One dimensional optical lattices

2.3.1 Far off-resonant atom-light interaction

As described in section 2.1, on timescales where spontaneous emission can be neglected, two-level atoms exposed to laser radiation undergo coherent Rabi oscillations between the two levels. Starting with c_g and c_e as the time-dependent coefficients multiplying the eigenstate wavefunctions of the ground and excited state respectively, and assuming the atom starts in the ground state $c_g(t = 0) = 1$, we make the traditional transformation to the rotating frame:

$$c'_g(t) = c_g(t) \tag{2.5}$$

$$c'_e(t) = c_e(t)e^{-i\delta t}, \tag{2.6}$$

where δ is the detuning of laser light from resonance. In this frame, we can write the atom-light Hamiltonian in the $\begin{pmatrix} c'_g \\ c'_e \end{pmatrix}$ basis as:

$$H = \hbar \begin{pmatrix} -\delta/2 & \Omega/2 \\ \Omega/2 & \delta/2 \end{pmatrix}, \quad (2.7)$$

where Ω is the coupling strength, also known as the Rabi frequency. In the limit of no coupling, $\Omega = 0$, in the rotating frame the eigenenergies are $E_{\pm} = \pm\hbar\delta/2$. For non-zero coupling, finding the eigenvalues of H gives $E_{\pm} = \pm\hbar\sqrt{\delta^2 + \Omega^2}/2$. Therefore, the bare (without light) eigenenergies are shifted in the presence of the light.

For a far detuned laser beam, one expects that no absorption of the light will actually take place, and the atom will remain entirely in the ground state. Indeed, solving the Shroedinger equation with the above Hamiltonian

$$i\hbar \frac{d}{dt} \begin{pmatrix} c'_g \\ c'_e \end{pmatrix} = H \begin{pmatrix} c'_g \\ c'_e \end{pmatrix} \quad (2.8)$$

we obtain the oscillating excited state population

$$c'_e(t) = -i \frac{\Omega}{\sqrt{\Omega^2 + \delta^2}} \sin \left(\frac{\sqrt{\Omega^2 + \delta^2} t}{2} \right), \quad (2.9)$$

where the amplitude of the oscillation approaches zero in the limit $\Omega \ll \delta$. Thus, the only effect of the light in this regime is to shift the eigenenergies of the ground and excited states. Expanding the energies in the small parameter Ω/δ , we obtain the shifted energies $E_{\pm} = \pm\hbar\sqrt{\delta^2 + \Omega^2}/2 \approx \pm(\delta/2 + \Omega^2/4\delta)$. The shift from bare energy levels is thus

$$\Delta E_{\pm} = \pm\Omega^2/4\delta. \quad (2.10)$$

This laser intensity dependent energy shift is called the AC Stark shift, and is the basis of most laser created potentials for cold atoms.

For the ground state, and a red detuned laser beam (where the laser frequency is lower than the resonant frequency), this creates energy minima in locations of maximal laser intensity. For the lattice described in this chapter, as well as for the trapping of our atoms in the final stages of cooling, we use high power (up to 10 W) lasers with wavelength $\lambda_L = 1064$ nm.

2.3.2 Lattice Hamiltonian

Our 1-D optical lattice is created by retro-reflecting the $\lambda_L = 1064$ nm laser, creating a standing wave of light. Via the AC Stark shift, this creates a periodic potential for the atoms of the form

$$V = V_0 \sin^2(k_L x), \quad (2.11)$$

where $k_L = 2\pi/\lambda_L$ is the wavenumber associated with the lattice recoil momentum. The time-independent Hamiltonian, for some eigenenergy E_n , will be given by

$$-\frac{\hbar^2}{2m} \frac{d^2}{dx^2} \Psi_n(x) + V_0 \sin^2(k_L x) \Psi_n(x) = E_n \Psi_n(x). \quad (2.12)$$

Since the potential is spatially periodic, we can invoke Bloch's theorem [2]:

$$\Psi_{n,q} = e^{iqx} u_{n,q}(x), \quad (2.13)$$

where q is the crystal momentum restricted to $\pm \hbar k_L$, and $u_{n,q}(x)$ is the spatially varying part of the wavefunction. Plugging this in to the Hamiltonian, we obtain

$$-\frac{\hbar^2}{2m} \left(-q^2 + 2iq \frac{d}{dx} + \frac{d^2}{dx^2} \right) u_{n,q}(x) + V_0 \sin^2(k_L x) u_{n,q}(x) = E_n u_{n,q}(x). \quad (2.14)$$

Expanding $u_{n,q}(x)$ in Fourier components commensurate with the lattice period of $2k_L$ as $u_{n,q}(x) = \sum_{j=-\inf}^{\inf} a_j e^{i2k_L j x}$, we obtain

$$\sum_j \left(\frac{\hbar^2}{2m} (q + 2k_L)^2 a_j + V_0 \sin^2(k_L x) a_j \right) e^{i2k_L j x} = E_n \sum_j a_j e^{i2k_L j x}. \quad (2.15)$$

Re-writing $\sin^2(k_L x) = (e^{-2ik_L x} + e^{2ik_L x} - 2)/4$, multiplying both sides by $e^{i2k_L j' x}$ and invoking $\sum_j c_j e^{ik(j-j')} = \delta_{jj'}$, where $\delta_{jj'}$ is the Kroniker delta and c_j are appropriately normalized coefficients, we get for any value of the index j

$$\frac{\hbar^2}{2m} (q + 2k_L j)^2 a_j - \frac{V_0}{4} (a_{j+1} + a_{j-1}) = E_n a_j. \quad (2.16)$$

This can be expressed in matrix form

$$H_L = \begin{pmatrix} \ddots & & & & & \\ & \frac{\hbar^2}{2m} (q + 4k_L)^2 & \frac{V_0}{4} & 0 & 0 & 0 \\ & \frac{V_0}{4} & \frac{\hbar^2}{2m} (q + 2k_L)^2 & \frac{V_0}{4} & 0 & 0 \\ & 0 & \frac{V_0}{4} & \frac{\hbar^2}{2m} q^2 & \frac{V_0}{4} & 0 \\ & 0 & 0 & \frac{V_0}{4} & \frac{\hbar^2}{2m} (q - 2k_L)^2 & \frac{V_0}{4} \\ & & 0 & 0 & \frac{V_0}{4} & \frac{\hbar^2}{2m} (q - 4k_L)^2 \\ & & & & & \ddots \end{pmatrix}, \quad (2.17)$$

in the basis of momentum orders $|k\rangle = e^{ikx}$ given by:

$$\begin{pmatrix} \vdots \\ |q + 4k_L\rangle \\ |q + 2k_L\rangle \\ |q\rangle \\ |q - 2k_L\rangle \\ |q - 4k_L\rangle \\ \vdots \end{pmatrix}. \quad (2.18)$$

This matrix can be diagonalized for every value of the crystal momentum q , with the resulting band structure shown in Figure 2. It is convenient to define the lattice recoil energy $E_L = \hbar^2 k_L^2 / 2m$. Then, we can re-write the Hamiltonian with V_0 in units of E_L and momenta q in units of k_L as

$$H_L/E_L = \begin{pmatrix} \ddots & & & & & \\ & (q+4)^2 & \frac{V_0}{4} & 0 & 0 & 0 \\ & \frac{V_0}{4} & (q+2)^2 & \frac{V_0}{4} & 0 & 0 \\ & 0 & \frac{V_0}{4} & q^2 & \frac{V_0}{4} & 0 \\ & 0 & 0 & \frac{V_0}{4} & (q-2)^2 & \frac{V_0}{4} \\ & & 0 & 0 & \frac{V_0}{4} & (q-4)^2 \\ & & & & & \ddots \end{pmatrix}. \quad (2.19)$$

In any numerical simulation, the number of momentum orders that can be included is finite. We determine the value of the parameter $n = \max(|j|)$ as the lowest n at which the eigenvalues stop changing to machine precision from $n - 1$. The code for finding and plotting the eigenvalues and eigenvectors of the lattice hamiltonian is included in Appendix [MAKE APPENDIX WITH CODE?].

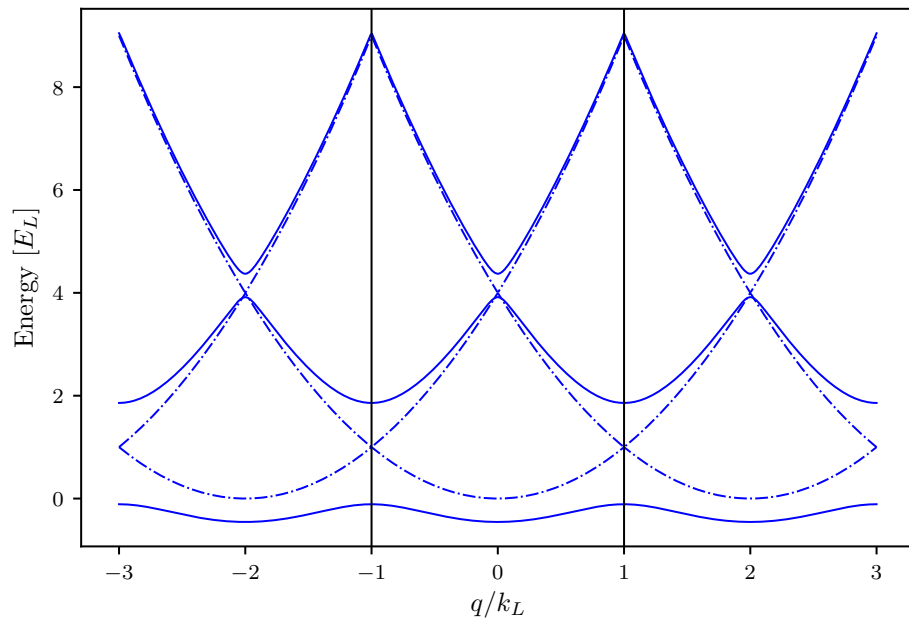


Figure 2: Lattice band structure in the extended zone scheme. The dashed lines represent the limit of zero lattice depth, with the regular parabolic dispersion relation of a free particle repeating with reciprocal lattice period. The solid lines are the dispersion relation at $V_0 = 4.0E_L$, showing the opening of gaps at crossings of the zero lattice depth bands. The black lines demarcate the first Brillouin zone.

2.3.3 Tight binding approximation

In the limit of large lattice depths, $V_0 > \approx 5E_L$, the lattice Hamiltonian is well approximated by the tight-binding model. In the tight binding model, the basis is assumed to be a set of orthogonal functions, called Wannier functions, localized to each lattice site $|j\rangle$. The approximation lies in assuming only nearest neighbor tunnelings between the sites, forming the tight-binding Hamiltonian

$$H_{\text{tb}} = -t |j\rangle \langle j+1| + \text{H.c.}, \quad (2.20)$$

where t is the tunneling amplitude between nearest neighbor sites and H.c. stands for Hermitian conjugate. We have neglected the diagonal kinetic energy term, as it will be equal for every Wannier function $|j\rangle$ and thus represents a constant energy offset. All the information about the lattice depth is therefore reflected in the tunneling amplitude t .

The tight binding Hamiltonian can also be expressed in the momentum basis by Fourier transforming the basis functions:

$$|j\rangle = \frac{1}{\sqrt{N}} \sum_{k_j} e^{-ik_j j} |k_j\rangle, \quad (2.21)$$

giving the Hamiltonian

$$H_{\text{tb}} = -\frac{1}{N} \sum_{k_1} \sum_{k_2} k_2 t e^{-ij k_1} e^{ik_2(j+1)} |k_1\rangle \langle k_2| + \text{H.c} = 2t \cos(k) |k\rangle \langle k|. \quad (2.22)$$

From this we can directly read off the band structure of the tight binding Hamiltonian. First, we notice that we only obtain one band - to approximate higher bands with the tight binding approximation we would need to construct a different set of Wannier functions and a different tunneling strength. Second, we see that the lowest

band is simply a cosine - therefore we have solved for the band structure without even defining what the basis Wannier functions are! Third, the amplitude of the cosine function is given by the tunneling strength t . This gives us a good clue as to how to determine the appropriate tunneling given a lattice depth V_0 - simply find a t that matches the amplitude of the lowest band, which becomes cosinusoidal in the deep lattice limit.

The precise form of the Wannier functions depends on both the depth of the lattice and the band being reproduced. It is not necessary for us to find their full expression, as the band structure can be calculated without them. The definition, however, is

$$|j\rangle = \int_{\text{BZ}} e^{i\phi(q)-iqja} \Psi_q(x) dq, \quad (2.23)$$

where the integral is over the Brillouin zone, from $-k_L$ to k_L , a is the lattice spacing $\lambda_L/2$, and Ψ_q is the Bloch wavefunction at crystal momentum q , and $\phi(q)$ is the phase associated with each Bloch wavefunction. The Bloch wavefunctions individually have arbitrary phase. The phase plays an important role in combining the Bloch wavefunctions into a Wannier function, finding the proper phase relationship to make the wavefunction maximally localized at each site [3].

2.3.4 Pulsing vs adiabatic loading of the lattice

The lattice depth parameter $V_0/4$, for a range of values, can be well calibrated experimentally by pulsing on the lattice. Here, the word pulsing indicates that the lattice is turned on fully non-adiabatically, if not instantaneously, such that the original bare momentum state is projected onto the lattice eigenbasis, as shown in Figure 5a. If the atoms start out stationary in the trap, the bare state in the

momentum basis is simply

$$|\Psi_0\rangle = \begin{pmatrix} \vdots \\ 0 \\ 0 \\ 1 \\ 0 \\ 0 \\ \vdots \end{pmatrix}, \quad (2.24)$$

as depicted in Figure 5b.

Since the lattice eigenbasis is distinct from the bare one, instantaneously turning on the lattice will necessarily excite the atoms into a superposition of lattice eigenstates, each evolving with a different phase according to the eigenenergy while the lattice is on, as shown in Figure 5c. Then, when the lattice is snapped back off, the wavefunction is projected back into the bare basis, and the varying phase accumulation results in a beating of the different momentum orders, see Figure 5d. This can be calculated simply by using the time evolution operator

$$|\Psi(t)\rangle = e^{-iH_L t/\hbar} |\Psi_0\rangle. \quad (2.25)$$

By pulsing on the lattice for variable amounts of time t , we can obtain fractional populations in the different momentum states. Time-of-flight imaging captures the momentum distribution of the cloud, and the different entries of $\Psi(t)$ in the momentum basis will thus appear as different clouds on the absorption image, as shown in Figure 4a. The fractional population in these clouds corresponds to a measurement of $|a_j|^2$. Typically for our values of the lattice depth $V_0 < 10E_L$, it is sufficient to simply count three central momentum orders, $k = q, q \pm 2k_L$. Then, we can fit Eq. 2.25 to the data with fitting parameter V_0 , thus deducing the lattice depth. Some

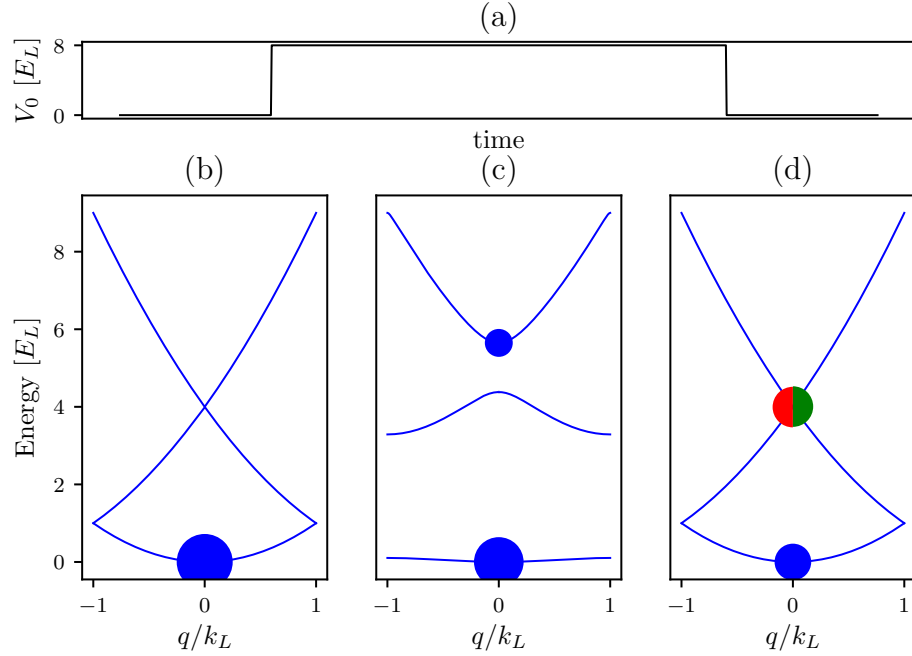


Figure 3: Lattice pulsing. (a) Lattice depth as a function of time during a pulsing experiment. The lattice is turned on instantaneously at $t = 0$ and held on for a variable amount of time until being turned off instantaneously at a final time $t = t_f$. (b) Atomic population before $t = 0$. The dispersion relation is that of a free particle, and all of the atoms start out at $q = 0$ in the lowest energy level. Here, the area of the dots is proportional to the fractional population in the energy state. (c) Atomic population after the lattice is turned on for a lattice depth of $V_0 = 8.0 E_L$. The energy spectrum now shows the lattice band structure, and some atomic population is projected onto the excited bands. (d) Atomic population after the lattice is snapped off at $t_f = 150 \mu s$. The wavefunction is projected back onto the bare states, with some fraction (blue circle) in the lowest band at $k = 0$ and some fraction in the excited band, with equal population being projected onto the $k = 2k_L$ (green) and $k = -2k_L$ (red).

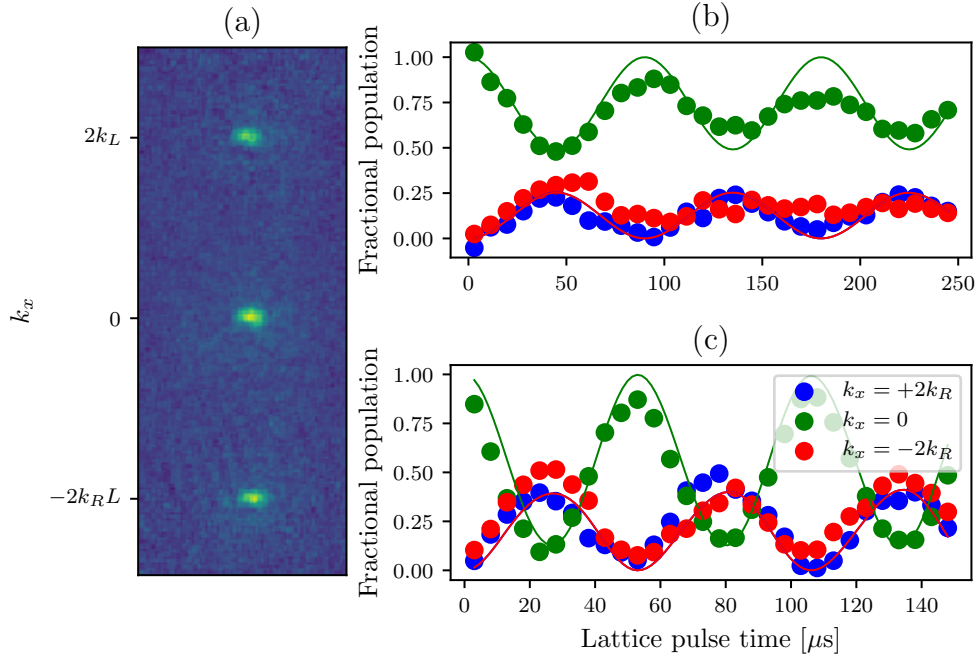


Figure 4: Lattice pulsing for calibration. (a) An example time-of-flight image from a pulsing experiment. The three different clouds are different momentum orders. (b) Fractional populations in the different momentum orders as a function of pulsing time at a low lattice power. Data is indicated by dots and best fit theory is represented by lines. The lattice depth from fit is $V_0 = 5.57 \pm 0.07 E_L$. (c) Fractional populations in the different momentum orders as a function of pulsing time at a higher lattice power. Data is indicated by dots and best fit theory is represented by lines. The lattice depth from fit is $V_0 = 12.69 \pm 0.07 E_L$.

examples of these pulsing experiments are presented in figure 4b,c.

In contrast to pulsing, adiabatic loading turns the lattice on slowly, such that the atomic wavefunction starting in the bare ground state can continuously adjust to remain in the ground state of the current Hamiltonian, without projecting onto any of the higher bands. This process is illustrated in Figure 5. The adiabatic timescale depends on the spacing between the ground and next excited band (or if starting in a different eigenstate, the nearest eigenstate). If the energy difference between the ground and first excited state is ΔE , the timescale on which the lattice is turned on must fulfill $t \gg \hbar/\Delta E$.

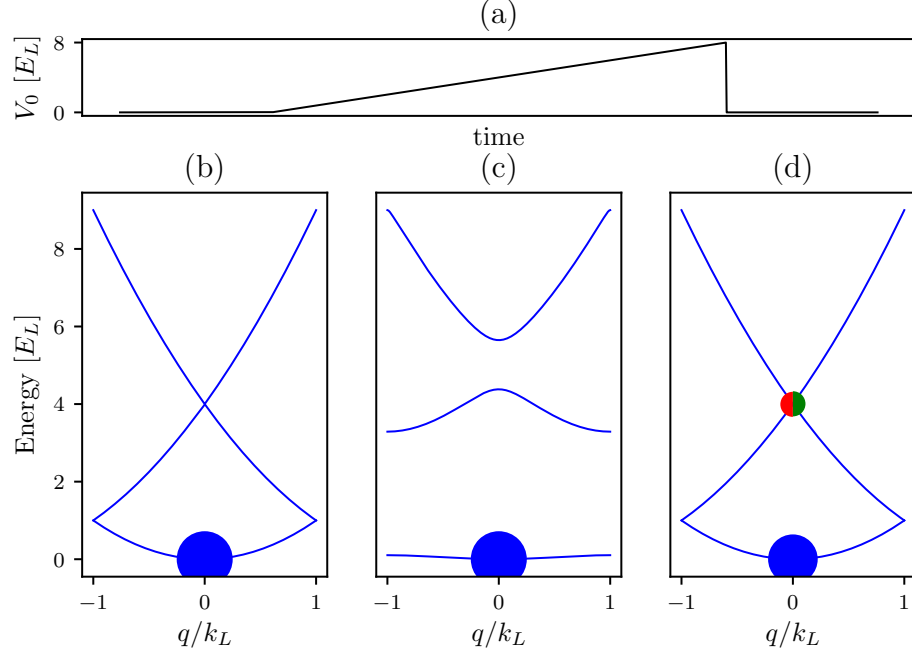


Figure 5: Adiabatic lattice loading. (a) Lattice depth as a function of time during adiabatic turn-on. The lattice is ramped on starting at $t = 0$, slowly increasing to a final lattice depth and turned off instantaneously at a final time $t = t_f$. (b) Atomic population before $t = 0$. All atoms are at $k = 0$ in the lowest bare band. (c) Atomic population after the lattice is turned on adiabatically to a lattice depth of $V_0 = 8.0E_L$. All atoms remain in the lowest band, but the band is no longer bare. (d) Atomic population after the lattice is snapped off. The wavefunction is projected back onto the bare states, with some fraction (blue circle) in the lowest band at $k = 0$ and some fraction in the excited band, with equal population being projected onto the $k = 2k_L$ (green) and $k = -2k_L$ (red). Since the lowest lattice band is a superposition of bare bands, some atoms are excited to the higher bare bands.

2.4 Raman and rf coupling

2.4.1 Hyperfine structure

Alkali atoms' energy levels can be understood as primarily the energy state of the single electron in the outer shell. Fine structure arises from different combinations of angular momenta, including orbital angular momentum of the outermost electron with respect to the nucleus \mathbf{L} , the electron spin \mathbf{S} and the nuclear spin \mathbf{I} . The total electron angular momentum is the combination of orbital and the spin angular momenta $\mathbf{J} = \mathbf{L} + \mathbf{S}$, and the quantum number can be any integer $|L - S| \leq J \leq |L + S|$. The ground state of ^{87}Rb , in term notation $^{2S+1}L_J$ is $^2S_{1/2}$, where S is orbital notation indicating $L = 0$. Since the total spin quantum number $J = 1/2$, this produces two possible spin projection quantum numbers, $m_J = \pm 1/2$.

There is also a contribution from the nuclear spin \mathbf{I} , resolvable at low magnetic fields, which gives rise to hyperfine structure of the states. For ^{87}Rb , $I = 3/2$. The total spin, including nuclear spin, is indicated by the quantum number F , and $|J - I| \leq F \leq |J + I|$. The interaction with the nuclear spin splits the ground state of ^{87}Rb into two manifolds, $F = 1$ and $F = 2$, with three hyperfine states in the $F = 1$ manifold ($m_F = 0, \pm 1$) and five hyperfine states in the $F = 2$ manifold ($m_F = 0, \pm 1, \pm 2$). These states couple to an external magnetic field B_z along some direction \mathbf{e}_z via the Hamiltonian $H_B = \mu_B(g_J J_z + g_I I_z)B_z/\hbar$. Here μ_B is the Bohr magneton, and g_J and g_I are Lande g-factors. Since $g_J \gg g_I$, at high fields the nuclear spin interaction becomes small compared to the total energy shift, and the levels are grouped according to their m_J quantum number, as seen in Figure 6.

At low fields, however, the states are approximately linearly dependent on the m_F quantum number. The linear shift from the $B = 0$ states is known as the linear Zeeman shift. In the intermediate regime, the correction to the linear shift can be expressed in terms of an energy correction to each hyperfine state $\epsilon(B)|m_F|^2$,

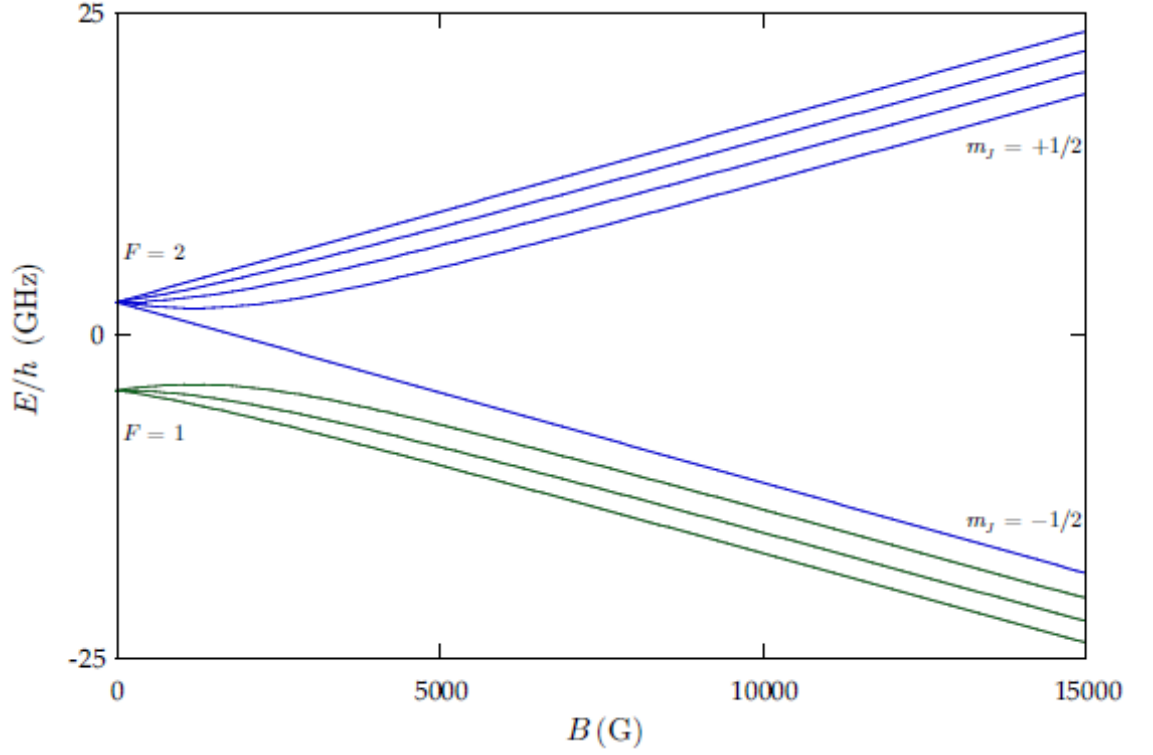


Figure 6: Energy structure of hyperfine states of the ground state of ^{87}Rb as a function of external magnetic field strength in Gauss. Figure from ref. [4]

known as the quadratic Zeeman shift. For the magnetic fields used in experiments described in this thesis, this correction is sufficient for describing the energy levels.

The form of the Hamiltonian in this regime for any value of F is given by

$$H_0 = H_{\text{KE}} + \hbar\omega_z \mathbf{F}_z + \hbar\epsilon \mathbf{F}_z^2, \quad (2.26)$$

where $\hbar\omega_z = \mu_B g_F B_z / \hbar$, and the kinetic energy Hamiltonian $H_{\text{KE}} = \hbar^2 \vec{k}^2 / 2m\mathcal{I}$, and \mathcal{I} is the identity matrix.

2.4.2 Rf coupling Hamiltonian

For the $F = 1$ manifold, there are three available spin states $m_F = 0, \pm 1$. There are many ways of introducing coupling terms between the different hyperfine states. Here, we will explain two methods: rf coupling and Raman coupling. Rf coupling is a radio-frequency oscillating magnetic field, in our case produced by a pair of circular coils in series side by side above the atoms (see [5]). Assuming the rf oscillating field is polarized along the \mathbf{e}_x , with the bias field along \mathbf{e}_z , the coupling Hamiltonian is given by $H_{rf} = \mu_B g_F \vec{\mathbf{F}} \cdot \vec{\mathbf{B}} = \mu_B g_F \mathbf{F}_x B_x \cos(\omega t)$, where $2\pi\omega$ is the rf frequency. The schematic of this setup is shown in Figure 7. The eigenstates of the bare Hamiltonian H_0 are the constituent m_F states. The eigenstates of the coupled Hamiltonian $H_0 + H_{rf}(t)$ can be expressed as a linear superposition of the bare eigenstates $\Psi(\vec{x}, t) = \sum_{m_F} c_{m_F}(t) \phi_{m_F}(\vec{x}) e^{-i\omega_{m_F} t}$. The Hamiltonian in this basis can then be written as [1]

$$H_{\text{rf}} = H_{\text{KE}} + \hbar \begin{pmatrix} 0 & \Omega \cos(\omega t) e^{i\omega_z t} & 0 \\ \Omega \cos(\omega t) e^{-i\omega_z t} & 0 & \Omega \cos(\omega t) e^{i\omega_z t} \\ 0 & \Omega \cos(\omega t) e^{-i\omega_z t} & 0 \end{pmatrix}, \quad (2.27)$$

where Ω is the Rabi frequency, proportional to B_x . We can then transfer into the rotating frame $c'_{m_F} = e^{-im_F \delta t} c_{m_F}$, where $\delta = \omega_z - \omega$. Then we apply the rotating wave approximation, that the fast oscillating terms average to zero over time scales of interest $e^{2i\omega t} \approx 0$, and obtain

$$H_{\text{rf}} = H_{\text{KE}} + \hbar \begin{pmatrix} \delta & \Omega/2 & 0 \\ \Omega/2 & -\epsilon & \Omega/2 \\ 0 & \Omega/2 & -\delta \end{pmatrix}, \quad (2.28)$$

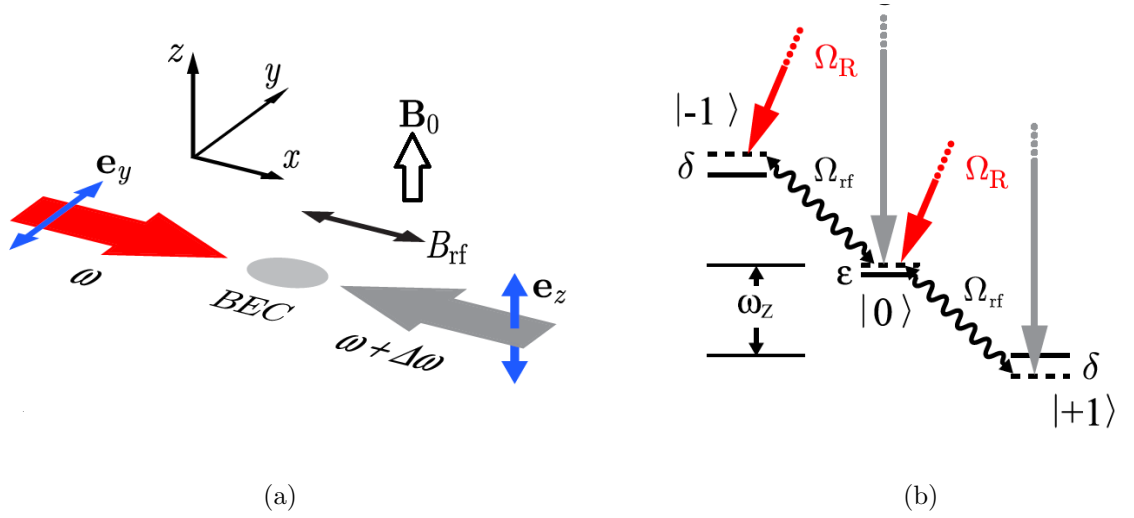


Figure 7: Raman and rf coupling schematic. (a) Beam geometry of the Raman beams and rf relative to the external field. The Raman beams have a frequency difference $\Delta\omega$, and are linearly polarized in perpendicular directions. (b) Level structure of both Raman and Rf coupling for hyperfine states of the $F = 1$ manifold. The hyperfine splitting separates the levels by an energy $\hbar\omega_z$. The quadratic Zeeman shift ϵ lowers the energy of the $m_F = 0$ state, and the detuning δ of either the Raman or the rf fields shifts the energies of the $m_F = \pm 1$ states. Raman transitions are two-photon, exciting up to a virtual state and coming back down to an adjacent hyperfine state, with an accompanying momentum transfer. Rf couples adjacent hyperfine states directly. Figure taken from ref. [6]

or for any value of F

$$H_{\text{rf}} = H_{\text{KE}} + \hbar\delta F_z + \hbar\epsilon F_z^2 + \Omega F_x/2. \quad (2.29)$$

The band structure of this Hamiltonian can be seen in Figure 8, where we have diagonalized Eq. 2.28 for a range of momenta k_x (we have isolated k_x for comparison with Raman coupling, as will be seen in the next section). The parabolas are simply the free particle dispersion relations along one dimension, with three bands arising from the three available spin states. It is convenient to define the magnetization of an eigenstate $m = \sum_{m_F} m_F * p_{m_F}$, where p_{m_F} is the fractional population in the m_F state. We have indicated the magnetization of the eigentate by coloring the

eigenenergies, with $m = -1$ in red, $m = 0$ in green, and $m = +1$ in blue. In Figure 8a, both the detuning and the coupling strength are zero. Therefore, there are simply three free particle dispersions, each exactly correlated with a particular spin state, the $m_F = \pm 1$ are degenerate and the $m_F = 0$ state is slightly offset by the quadratic shift $\hbar\epsilon$. In Figure 8c, the coupling strength is again zero, but the detuning has been turned on, lifting the degeneracy between the $m_F = \pm 1$ states. Figure 8b,d shows the same conditions as a,c, respectively, but with the coupling strength turned on. In Figure 8b, where the detuning is zero and the quadratic shift is negligible compared to the coupling strength, all states average to a magnetization of zero—the $m_F = \pm 1$ states are symmetrically populated. In Figure 8d, this symmetry is broken by the presence of a detuning.

2.4.3 Raman coupling Hamiltonian

The counter-propagating Raman beams, as seen in Figure 7, couple the same states as the rf. They do so via the vector light shift created by the pair of beams. The electric field due to the right going beam (red in Figure 7a) is $\mathbf{E} = E_0 \exp(ik_R x - i\omega t) \mathbf{e}_y$, where E_0 is the amplitude of the electric field and $\hbar k_R = h/\lambda_R = \hbar\omega/c$. The electric field from the left going beam (gray in Figure 7b) is $\mathbf{E} = E_0 \exp(-ik_R x - i(\omega + \Delta\omega)t) \mathbf{e}_z$. This combines to give an effective field from the vector light shift [7] $B_{\text{eff}} \propto \mathbf{E} \times \mathbf{E}^* \propto -E_0^2 \cos(2k_R x + \Delta\omega t) \mathbf{e}_x$. Going through the same procedure as for the rf coupling case, including the transfer into the rotating frame and the rotating wave approximation, we obtain the same Hamiltonian in the basis of bare spin states $| -1 \rangle, | 0 \rangle, | 1 \rangle$ but with an extra phase factor:

$$H_{\text{Raman}} = H_{\text{KE}} + \hbar \begin{pmatrix} \delta & \Omega/2 e^{-i2k_R x} & 0 \\ \Omega/2 e^{i2k_R x} & -\epsilon & \Omega/2 e^{-i2k_R x} \\ 0 & \Omega/2 e^{i2k_R x} & -\delta \end{pmatrix}, \quad (2.30)$$

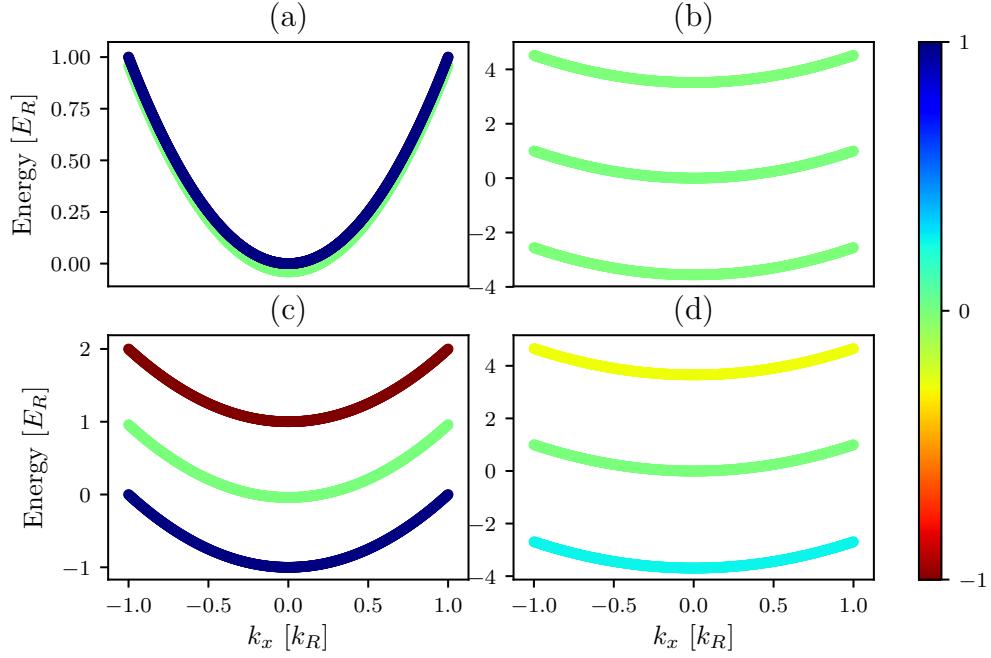


Figure 8: Band structure of the rf Hamiltonian, Eq. 2.28, in momentum space. For all plots, the quadratic Zeeman shift $\hbar\epsilon = 0.04E_R$, and the color represents magnetization, labeled by the colorbar. (a) $\hbar\Omega = 0$, $\hbar\delta = 0$. No coupling or detuning is present, so the only separation between the bands is due to the quadratic shift $\hbar\epsilon$. (b) $\hbar\Omega = 5.0E_R$, $\hbar\delta = 0$. (c) $\hbar\Omega = 0$, $\hbar\delta = 1.0E_R$. Even though the coupling strength is zero, the bands are separated by the detuning. (d) $\hbar\Omega = 5.0E_R$, $\hbar\delta = 1.0E_R$.

where $\delta = \omega_z - \Delta\omega$.

This phase difference between the rf and Raman Hamiltonian has an intuitive physical explanation. In order to undergo a Raman transition, an atom first absorbs a photon from one beam, getting a momentum kick equal to the recoil momentum $\hbar k_R$. Then, to decay back down to an adjacent spin state, the undergoes stimulated emission into the field of the other (counter-propagating) beam, acquiring another recoil momentum kick in the same direction for a total of $2\hbar k_R \mathbf{e}_x$. Therefore, the Raman coupling Hamiltonian for $F = 1$, after transforming into the rotating frame and performing the rotating wave approximation, can be written in the same way as the rf Hamiltonian in Eq. 2.28 with the addition of a momentum kick—in real space, an acquired phase—of $e^{i2k_R x}$.

We can again make a basis transformation to get rid of this phase. Let us define $|-1\rangle' = \exp(-2ik_R x)|-1\rangle = |k_x - 2k_R, -1\rangle$, $|0\rangle' = |0\rangle = |k_x, 0\rangle$, $|1\rangle' = \exp(2ik_R x)|1\rangle = |k_x + 2k_R, 1\rangle$, where for third definition we went into the momentum basis and labelled the states by a combination of their momentum and spin state. Then, including the kinetic energy term along \mathbf{e}_x explicitly, we obtain the Hamiltonian in the new basis as:

$$H_{\text{Raman}} = H_{\text{KE}}^{(y,z)} + \begin{pmatrix} \frac{\hbar^2(k_x - 2k_R)^2}{2m} + \hbar\delta & \hbar\Omega/2 & 0 \\ \hbar\Omega/2 & \frac{\hbar^2 k_x^2}{2m} - \hbar\epsilon & \hbar\Omega/2 \\ 0 & \hbar\Omega/2 & \frac{\hbar^2(k_x + 2k_R)^2}{2m} - \hbar\delta \end{pmatrix}. \quad (2.31)$$

It is convenient to define the Raman recoil energy as $E_R = \frac{\hbar^2 k_R^2}{2m}$. The band structure of this Hamiltonian is shown in Figure 9, for several representative parameter values, with the magnetization labelled by the color. Figure 9a shows the band structure in the limit of zero coupling and zero detuning, but where we have already gone into the basis $|k_x - 2k_R, -1\rangle, |k_x, 0\rangle, |k_x + 2k_R, 1\rangle$; therefore, the free particle parabola corresponding to the $m_F = 1$ spin states is shifted to center on

$k_x = -2k_R$ and the $m_F = -1$ parabola is shifted to center on $k_x = 2k_R$. As the coupling is turned on to $\hbar\Omega = 1E_R$ in Figure 9b, the points where the parabolas cross become 'avoided crossings', separating into three bands where magnetization (and the underlying spin distribution) depends on the momentum k_x . As the coupling strength is turned up even further to $\hbar\Omega = 5E_R$ in Figure 9c, the lowest band goes from having three minima, one corresponding to each original spin state, to only one minimum. This transition happens at $\hbar\Omega = 4E_R$ [5]. In Figure 9d, we show the band structure again in the limit of zero coupling, but this time with a detuning of $\hbar\delta = 1.0E_R$. Note that the detuning tips the parabolas with respect to each other. Figure 9e shows the detuned system with coupling strength turned up to $\hbar\Omega = 1E_R$, still in the three minima regime but with avoided crossings creating three momentum and spin coupled bands. In Figure 9f, the detuned system is turned up to a coupling strength of $\hbar\Omega = 5E_R$, creating a single minimum, this time offset from $k_x = 0$.

We can write the general F version of the Raman coupled Hamiltonian in the basis $|k_x + m_F * 2k_R, m_F\rangle$, where $-F \leq m_F \leq F$, as:

$$H_{\text{Raman}} = H_{\text{KE}}^{(y,z)} + \hbar^2(k_x\mathcal{I} + 2k_R F_z)^2/2m + \hbar\delta F_z + \hbar\epsilon F_z^2 + \Omega F_x/2. \quad (2.32)$$

2.4.4 Calibration of Raman and Rf dressed states

To calibrate the rf and Raman coupling strengths, we take a similar approach to the 1-D lattice calibration: start in a pure spin state, for example $m_F = 0$, and turn the coupling on non-adiabatically to induce Rabi oscillations between the coupled states. Then, during time-of-flight, apply a Stern-Gerlach gradient pulse to separate the spin components and observe the fractional populations in different spin states as a function of Rabi oscillation time.

Figure 10a,b shows example images obtained in time-of-flight when pulsing on

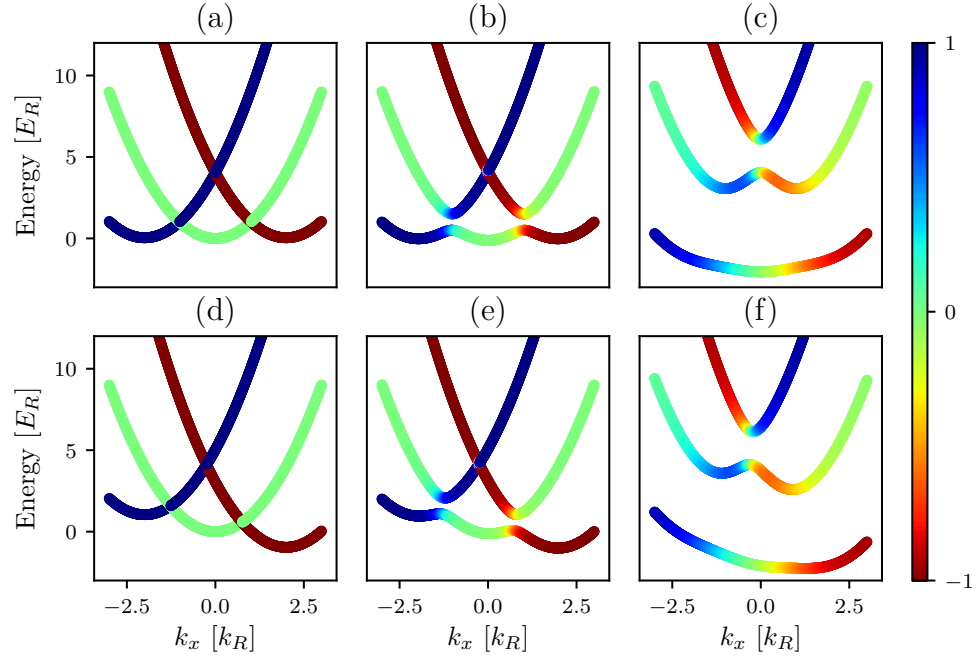


Figure 9: Band structure of the Raman Hamiltonian, Eq. 2.31, in momentum space. For all plots, the quadratic Zeeman shift $\hbar\epsilon = 0.04E_R$, and the color represents magnetization, labeled by the colorbar. (a) $\hbar\Omega = 0$, $\hbar\delta = 0$. (b) $\hbar\Omega = 1.0E_R$, $\hbar\delta = 0$. (c) $\hbar\Omega = 5.0E_R$, $\hbar\delta = 0$. (d) $\hbar\Omega = 0.0$, $\hbar\delta = 1.0E_R$. (e) $\hbar\Omega = 1.0E_R$, $\hbar\delta = 1.0E_R$. (f) $\hbar\Omega = 5.0E_R$, $\hbar\delta = 1.0E_R$

an rf coupling field for atoms in the $F = 1$ and $F = 2$ manifold, respectively. The Stern-Gerlach gradient pulse separates the spin components along the horizontal axis in the images. The fractional population in each state can then be obtained by summing up the optical depth in each cloud and dividing by the total optical depth. Similarly, Figure 11a shows an example time-of-flight image obtained when pulsing on a Raman coupling field on an $F = 1$ cloud initially in the $m_F = 0$ spin state. Here, the spin states are separated along the horizontal axis by the same Stern-Gerlach pulse. In addition, the recoil momentum obtained when undergoing a Raman transition separates the different spin states along the vertical axis—parallel to the Raman beams along \mathbf{e}_x . The direction of the Stern-Gerlach gradient was chosen purposefully to be perpendicular to the Raman direction \mathbf{e}_x for easy separation of the two effects.

These population oscillations can then be fit for coupling strength $\hbar\Omega$ and detuning $\hbar\delta$. Note that the quadratic Zeeman shift $\hbar\epsilon$ is set by the strength of the bias field B_0 and therefore often well known - we do not fit for this. The theoretic predictions are obtained by applying the time evolution operator $U = \exp(-iH_{\text{Raman/rf}}t/\hbar)$ to an initial state Ψ in the appropriate basis. Figure 10c shows an example time series of rf pulsing in the $F = 1$ manifold, starting in the $m_F = 0$ state. The lines of best fit are overlayed on experimental data, extracting fit parameters $\hbar\Omega = 0.863 \pm 0.004E_R$ and $\hbar\delta = -0.198 \pm 0.007E_R$. Figure 10d shows an example time series of rf pulsing in the $F = 2$ manifold, starting in the $m_F = -2$ state. Here, the extracted fit parameters were $\hbar\Omega = 1.000 \pm 0.002E_R$ and $\hbar\delta = -0.061 \pm 0.001E_R$.

Figure 11b shows an example time series of Raman pulsing in the $F = 1$ manifold, starting in the $m_F = 0$ state, with fitted parameters $\hbar\Omega = 1.47 \pm 0.01E_R$ and $\hbar\delta = 0.004 \pm 0.024E_R$. Note that although the coupling strength is almost double the rf coupling strength in Figure 10c, the contrast (peak to peak oscillation

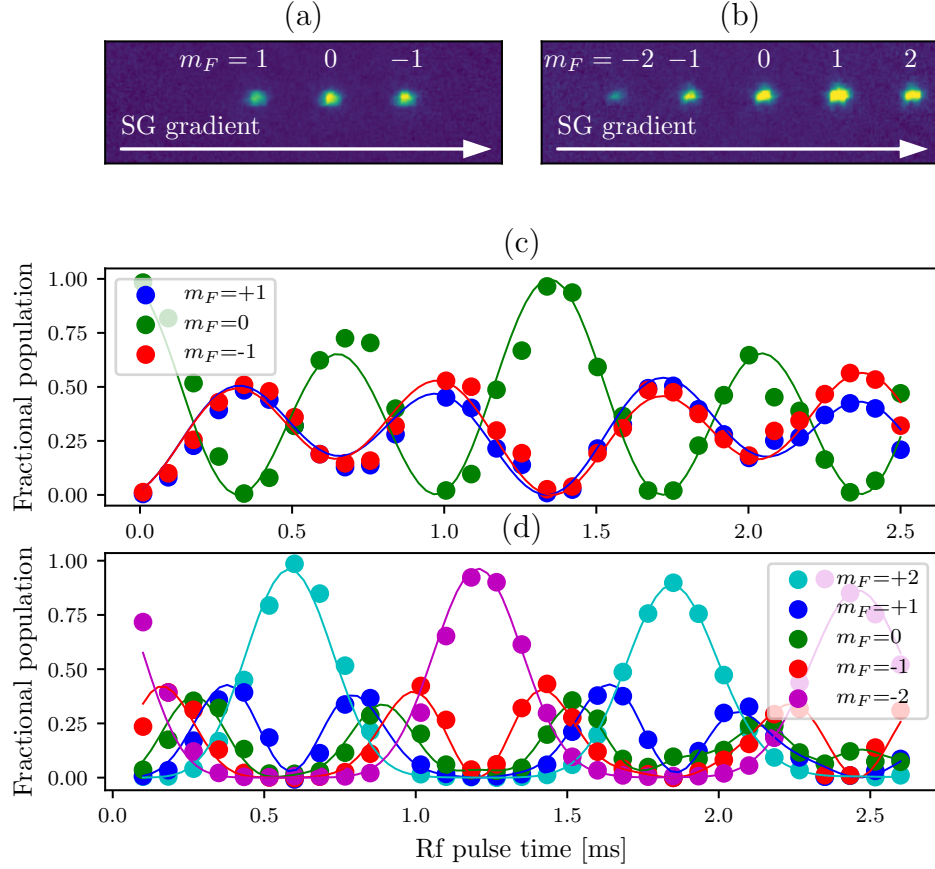


Figure 10: Pulsing on rf coupling. (a) Example time-of-flight image during an rf pulsing experiment in the $F = 1$ manifold. Spin states are separated via a Stern-Gerlach pulse along the horizontal direction. (b) Example time-of-flight image during an rf pulsing experiment in the $F = 2$ manifold. Here, 5 spin components are present. (c) Pulsing experiment in the $F = 1$ manifold. Dots represent fractional populations in different spin states measured from time-of-flight images, and lines represent best fit theory curves. Fitted parameters are $\hbar\Omega = 0.863 \pm 0.004E_R$, $\hbar\delta = -0.198 \pm 0.007E_R$. (d) Pulsing experiment in the $F = 2$ manifold. Dots represent fractional populations in different spin states measured from time-of-flight images, and lines represent best fit theory curves. Fitted parameters are $\hbar\Omega = 1.000 \pm 0.002E_R$, $\hbar\delta = -0.061 \pm 0.001E_R$. $\hbar\epsilon = 0.038E_R$ for all panels.

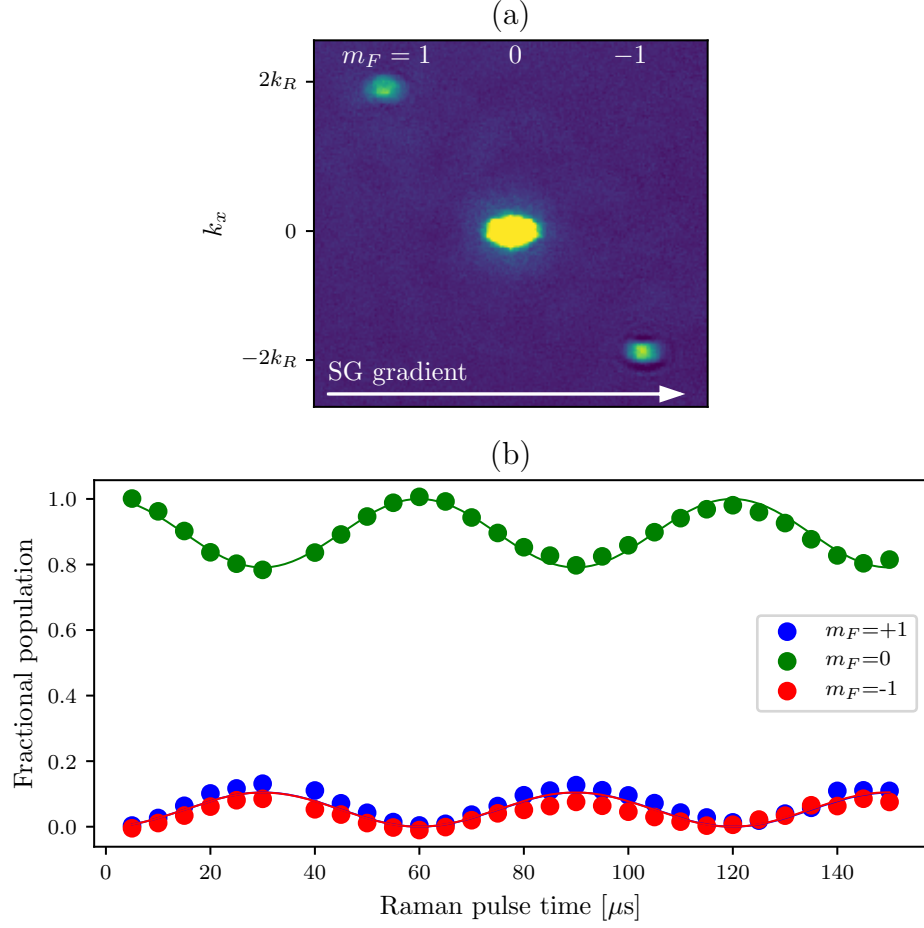


Figure 11: Pulsing on Raman coupling. (a) Example time-of-flight image during a Raman pulsing experiment in the $F = 1$ manifold. A Stern-Gerlach pulse during time-of-flight separates different spin components along the horizontal direction, and different momentum orders fly apart along the vertical direction. (b) Fractional population in different spin states during a Raman pulsing experiment as a function of time. Dots represent data and lines represent a best fit from theory. The fitted parameters are $\hbar\Omega = 1.47 \pm 0.01 E_R$, $\hbar\delta = 0.004 \pm 0.024 E_R$. The quadratic Zeeman shift was $\hbar\epsilon = 0.038 E_R$.

of the fractional population in, say, the $mF = 0$ state) is much lower in the Raman data than in the rf. This is a direct consequence of the recoil momentum transfer, and can be understood by looking at the band structure. For rf, the coupled bands at initial momentum $k_x = 0$ are separated by the coupling strength, see Figure ??b. For Raman, even at zero coupling strength, due to the shifting of the parabolas by $2k_R$, and $k_x = 0$ the higher bands are $\hbar^2(2k_R)^2/2m = 4E_R$ separated from the lower bands. Therefore, the energy difference is larger and the fraction in the excited band will be lower, leading to lower contrast.

Chapter 6: Synthetic Magnetic Fields in Synthetic Dimensions

In condensed matter, 2-D systems in high fields have proved to be of great technological use and scientific interest. The integer quantum Hall effect (IQHE) [8], with its quantized Hall resistance, had given rise to an ultra-precise standard for resistivity. It was also one of the first examples of topology playing an important role in physics—the precise quantization of the Hall conductance is guaranteed by the non-trivial topology of the system [9]. This quantizes the magnetic flux into flux quanta of $\Phi_0 = 2\pi\hbar/e$, where e is the electron charge, and leads to a new ‘plateau’ in the resistivity when an additional quantum of flux is threaded through the system.

In the IQHE system, the underlying lattice structure of metal is effectively washed out—the magnetic flux per individual lattice plaquette is negligible. However, new physics arises when the magnetic flux per plaquette is increased to some non-negligible fraction of the flux quantum, giving rise to the Hofstadter butterfly [10]. These regimes are hard to reach experimentally, since the typical plaquette size in crystalline material is of order a square angstrom, and the magnetic field necessary to thread create a magnetic flux of Φ_0 through such a narrow area is of order $\approx 10^4$ Tesla, not accessible with current technology.

Several platforms have, however, reached the Hofstadter regime by engineering systems with large effective plaquette size, in engineered materials [11, 12], and in atomic [13–18] and optical [19] settings. Here, we use the approach of synthetic dimensions [20] to reach the Hofstadter regime. We demonstrate the non-trivial topology of the system created, and use it to image skipping orbits at the edge of

the 2-D system—a hallmark of 2-D electron systems in a semiclassical treatment.

The work described in this chapter was published in [21].

6.1 Synthetic dimensions setup

Any internal degree of freedom can be thought of as a synthetic dimension—the different internal states can be treated as sites along this synthetic direction. As long as there is some sense of distance along this direction, i.e. some of the internal states are 'nearest neighbors' while others are not, this is a meaningful treatment. In our case an effective 2-D lattice is formed by sites formed by a 1-D optical lattice along a 'real' direction, here \mathbf{e}_x , and the atom's spin states forming sites along a 'synthetic' direction, \mathbf{e}_s .

The experimental setup for this system is schematically represented in 1a. The BEC is subject to a 1-D optical lattice, formed by a retro-reflected beam of $\lambda_L = 1064nm$ along \mathbf{e}_x . A bias magnetic field B_0 along \mathbf{e}_z separates the different spin states. The spin states can be thought of as sites along a synthetic dimension even without any coupling field. However, only once a coupling field is present do they acquire a sense of distance. We couple them via rf or Raman coupling, which only couples adjacent spin states. The Raman beams illuminating the atoms are along the same \mathbf{e}_x direction as the 1-D optical lattice. The rf field has components both along the \mathbf{e}_x and \mathbf{e}_y .

Figure 1b sketches out the effective 2-D lattice created. Here, we have labelled the lattice sites along the 'real' direction \mathbf{e}_x by site index j . In the tight binding approximation, we can describe a lattice hopping between adjacent sites with tunneling amplitude t_x . Similarly, the sites along the 'synthetic' dimension are labelled by site index m (identical to spin projection quantum number m_F), and the rf or Raman coupling here plays the role of a tunneling amplitude t_s . In the case of rf coupling, there is no momentum kick associated with spin exchange, and both t_x

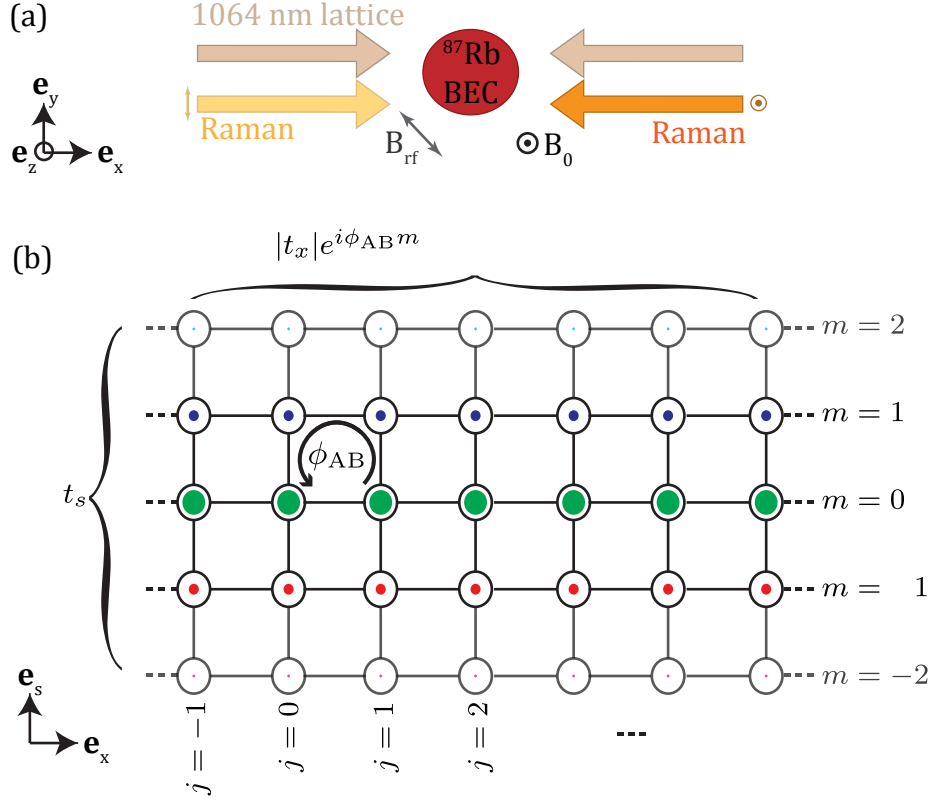


Figure 1: Setup of effective 2-D lattice. (a) Beam geometry. The BEC is subject to a bias magnetic field B_0 in the \mathbf{e}_z direction. The 1-D lattice beam and Raman beams are both along the \mathbf{e}_x direction, and the rf field can be applied with projections onto both the \mathbf{e}_x and \mathbf{e}_y . (b) Schematic of the effective 2-D lattice. Sites along \mathbf{e}_x are formed by the 1-D optical lattice and labelled by site number j . Sites along the synthetic direction \mathbf{e}_s are formed by the spin states: 3 sites for atoms in the $F = 1$ manifold and 5 sites for atoms in $F = 2$. These sites are labelled by m . Raman transitions induce a phase shift, which can be gauge transformed into a tunneling phase along the \mathbf{e}_x direction. This leads to a net phase when hopping around a single lattice plaquette of ϕ_{AB} .

and t_s are real.

In the case of Raman coupling, however, there is a momentum kick of $2k_R$ associated with every spin transfer, and therefore a phase factor of $\exp(2ik_R x)$ with every spin 'tunneling' event. Since position x is set by the 1-D lattice, $x_j = j\lambda_L/2 = j\pi/k_L$, and the space dependent phase factor is $\exp(2\pi i k_R/k_L j)$. An absolute phase change in the wavefunction is not meaningful. However, a phase acquired when going around a plaquette and coming back to the same place is meaningful, as one could imagine one atom staying at the same site and the other going around a plaquette and coming back to detect the phase difference. In this setup, the phases acquired while going around a single plaquette are, starting at some lattice site $|j, m\rangle$, are: 0 (for tunneling right to $|j+1, m\rangle$), $2\pi i k_R/k_L(j+1)$ (for tunneling up to $|j+1, m+1\rangle$), 0 (for tunneling left to $|j, m+1\rangle$) and $-2\pi i k_R/k_L j$ (for tunneling back down to $|j, m\rangle$). The total phase acquired is thus $\phi_{AB} = 2\pi k_R/k_L$, independent of the starting lattice site. Since the absolute phase does not matter and only the value of ϕ_{AB} , we can perform a phase transformation that shifts the tunneling phase onto the spatial direction, defining $t_x = |t_x|\exp(i\phi_{AB}m)$ and $t_s = |t_s|$, as labelled in Figure 1b.

To see how this phase implies an effective magnetic field, we draw an analogy to the Aharonov-Bohm effect [22, 23] from quantum mechanics. In this effect, consider an infinite solenoid with an electric current running through it. The magnetic field B in this setup exists only inside the solenoid, while the magnetic vector potential persists outside the solenoid. However, if two electrons are sent on a trajectory around the solenoid, even though they never pass through any magnetic field, they nevertheless acquire a relative phase that can be detected by interfering them with each other. This relative phase is given by $\phi_{AB} = 2\pi\Phi/\Phi_0$, where $\Phi = B * A$ is the magnetic flux through the solenoid (A is the area pierced by the magnetic field) and $\Phi_0 = h/e$ is the flux quantum, with e the electron charge. Since in our system,

the atoms acquire a phase when they perform a closed loop around a single lattice plaquette. Therefore, they behave as though there was an infinite solenoid piercing each plaquette with a magnetic field going through it, and the flux per plaquette in units of the flux quantum is $\Phi/\Phi_0 = \phi_{AB}/2\pi = k_R/k_L$. For the case of rf coupling, the phase acquired at every transition is 0 and the fluxss $\Phi/\Phi_0 = 0$.

6.2 Hamiltonian of the effective 2-D system

The full Hamiltonian of this system, without making the tight binding approximation, can be written down by combining the lattice Hamiltonian (eqn. 6.4) and the rf (eqn. 2.28) or Raman Hamiltonian (eqn. 2.31). To do this, we write a new basis that encompasses both the momentum and the spin degrees of freedom. For the lattice Hamiltonian, we used the momentum basis

$$\begin{pmatrix} \vdots \\ |q + 4k_L\rangle \\ |q + 2k_L\rangle \\ |q\rangle \\ |q - 2k_L\rangle \\ |q - 4k_L\rangle \\ \vdots \end{pmatrix}. \quad (6.1)$$

For the Raman Hamiltonian in the $F = 1$ manifold, we used the spin and momentum basis

$$\begin{pmatrix} |k_x - 2k_R, -1\rangle \\ |k_x, 0\rangle \\ |k_x + 2k_R, 1\rangle \end{pmatrix}. \quad (6.2)$$

In a lattice, the momentum k_x becomes crystal momentum q . For every state in the lattice basis, we now expand to three states, one for each spin state, with the

appropriate momentum shifts. We obtain

$$\begin{pmatrix} \vdots \\ |q + 2k_L - 2k_R, -1\rangle \\ |q + 2k_L, 0\rangle \\ |q + 2k_L + 2k_R, 1\rangle \\ |q - 2k_R, -1\rangle \\ |q, 0\rangle \\ |q + 2k_R, 1\rangle \\ |q - 2k_L - 2k_R, -1\rangle \\ |q - 2k_L, 0\rangle \\ |q - 2k_L + 2k_R, 1\rangle \\ \vdots \end{pmatrix}. \quad (6.3)$$

In this basis, we combine the lattice and Raman Hamiltonians (ommiting the kinetic energy in the other two directions) in an infinite block matrix form as

$$H = \begin{pmatrix} \ddots & & & \\ & \mathbf{H}_R(2k_L) & \frac{\mathbf{V}_0}{4} & \mathbf{0} \\ & \frac{\mathbf{V}_0}{4} & \mathbf{H}_R(0) & \frac{\mathbf{V}_0}{4} \\ & \mathbf{0} & \frac{\mathbf{V}_0}{4} & \mathbf{H}_R(-2k_L) \\ & & & \ddots \end{pmatrix}, \quad (6.4)$$

where $\mathbf{H}_R(x)$ is the Raman Hamiltonian with a momentum shift of x :

$$\mathbf{H}_R(x) = \begin{pmatrix} \frac{\hbar^2(q+x-2k_R)^2}{2m} + \hbar\delta & \hbar\Omega/2 & 0 \\ \hbar\Omega/2 & \frac{\hbar^2(q+x)^2}{2m} - \hbar\epsilon & \hbar\Omega/2 \\ 0 & \hbar\Omega/2 & \frac{\hbar^2(q+x+2k_R)^2}{2m} - \hbar\delta \end{pmatrix}, \quad (6.5)$$

the matrix $\frac{V_0}{4}$ is a 3x3 diagonal matrix lattice coupling strength $\frac{V_0}{4}$ on the diagonal, and $\mathbf{0}$ is a 3x3 matrix of zeros.

This Hamiltonian is easily extended to higher F values by replacing the Raman blocks $\mathbf{H}_R(x)$ with the corresponding Raman coupling Hamiltonian from eqn. 2.32, and extending the diagonal matrix $\frac{V_0}{4}$ and the zero matrix $\mathbf{0}$ to be $(2F+1) \times (2F+1)$.

Figure: Band structure, $F=1$ and $F=2$, with and without Raman coupling

par1: Write out full Hamiltonian

par2: Talk about band structure, periodic and spin dependent

par3: How we calibrate the synthetic dimensions system by pulsing

Figure: example TOF images, pulsing experiments for $F=1$ and $F=2$

par4: Write out tight binding version, explain how closely it applies. Figure: fits for effective tunneling amplitudes?

6.3 Eigenstates of the synthetic 2-D lattice

par1: 'Edge' and 'bulk' states of electrons in a magnetic field

par2: Explain loading procedure for adiabatic states

par3: Explain figure, magnetic length

6.4 Observation of skipping orbits

par1: Skipping orbits in 2-D electrons in a magnetic fields

par2: Experimental sequence for skipping orbits measurement

par3: How position is calculated from integrating velocity as a function of time. Explain figure

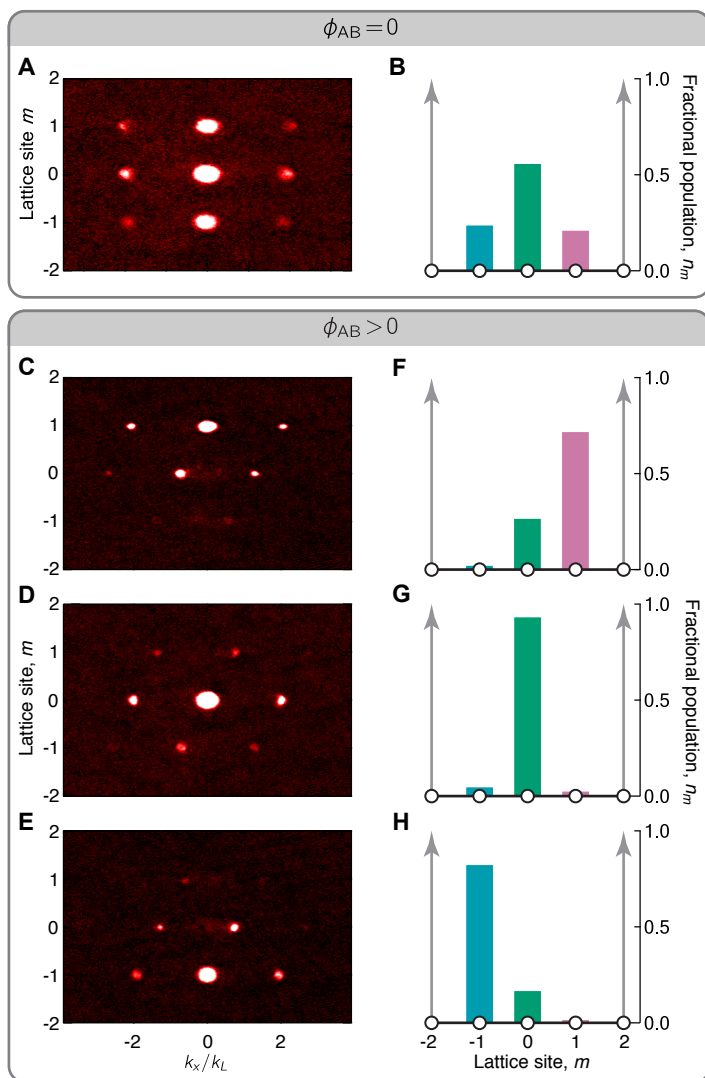


Figure 2:

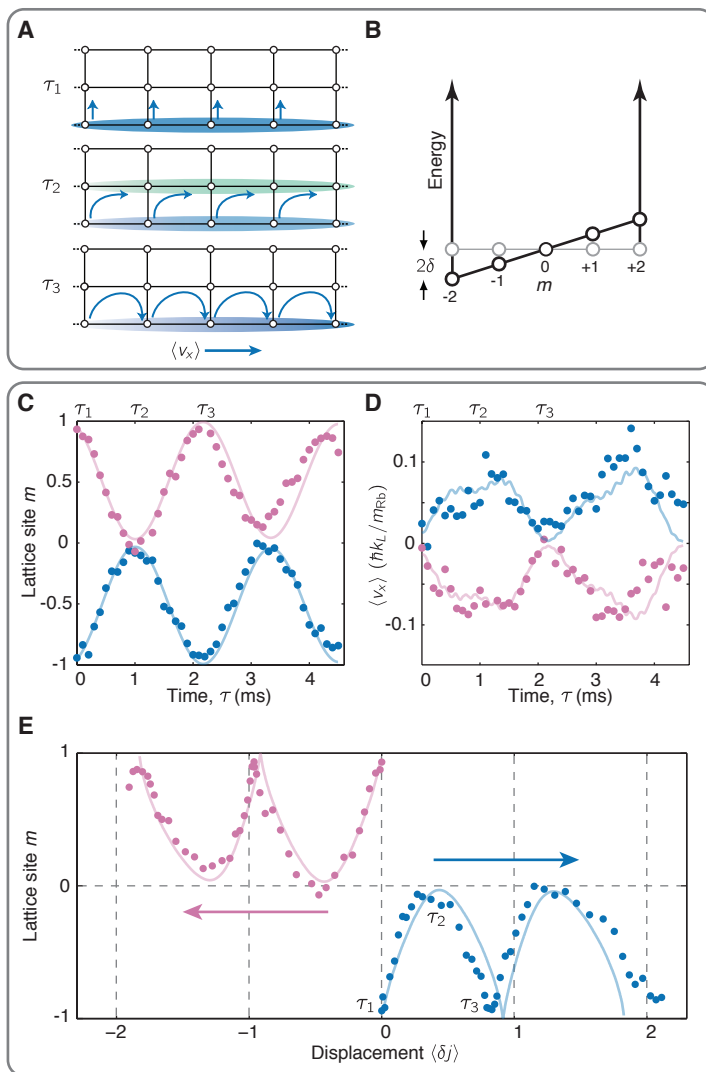


Figure 3:

Bibliography

- [1] H.J. Metcalf and P. van der Straten. *Laser Cooling and Trapping*. Graduate Texts in Contemporary Physics. Springer New York, 1999.
- [2] N.W. Ashcroft and N.D. Mermin. *Solid State Physics*. Saunders College, Philadelphia, 1976.
- [3] Nicola Marzari, Arash A. Mostofi, Jonathan R. Yates, Ivo Souza, and David Vanderbilt. Maximally localized wannier functions: Theory and applications. *Rev. Mod. Phys.*, 84:1419–1475, Oct 2012.
- [4] Daniel Adam Steck. Rubidium 87 d line data. Available online, <http://steck.us/alkalidata>, April 2018. revision 2.1.5.
- [5] Karina Jimenez-Garcia. *Artificial Gauge Fields for Ultracold Neutral Atoms*. PhD thesis, Joint Quantum Institute, National Institute of Standards and Technology, and the University of Maryland, 2012.
- [6] K. Jiménez-García, L. J. LeBlanc, R. A. Williams, M. C. Beeler, A. R. Perry, and I. B. Spielman. Peierls substitution in an engineered lattice potential. *Phys. Rev. Lett.*, 108:225303, May 2012.

- [7] Daniel Adam Steck. Quantum and atom optics. Available online at <http://steck.us/teaching>, January 2015. revision 0.12.2.
- [8] K. v. Klitzing, G. Dorda, and M. Pepper. New method for high-accuracy determination of the fine-structure constant based on quantized hall resistance. *Phys. Rev. Lett.*, 45:494–497, Aug 1980.
- [9] D. J. Thouless, M. Kohmoto, M. P. Nightingale, and M. den Nijs. Quantized hall conductance in a two-dimensional periodic potential. *Phys. Rev. Lett.*, 49:405–408, Aug 1982.
- [10] Douglas R. Hofstadter. Energy levels and wave functions of bloch electrons in rational and irrational magnetic fields. *Phys. Rev. B*, 14:2239–2249, Sep 1976.
- [11] M. C. Geisler, J. H. Smet, V. Umansky, K. von Klitzing, B. Naundorf, R. Ketzmerick, and H. Schweizer. Detection of a landau band-coupling-induced rearrangement of the hofstadter butterfly. *Phys. Rev. Lett.*, 92:256801, Jun 2004.
- [12] B. Hunt, J. D. Sanchez-Yamagishi, A. F. Young, M. Yankowitz, B. J. LeRoy, K. Watanabe, T. Taniguchi, P. Moon, M. Koshino, P. Jarillo-Herrero, and R. C. Ashoori. Massive Dirac Fermions and Hofstadter Butterfly in a van der Waals Heterostructure. *Science*, 340:1427, 2013.
- [13] P. Zoller D. Jaksch. Creation of effective magnetic fields in optical lattices: the hofstadter butterfly for cold neutral atoms. *New Journal of Physics*, 5(1):56, 2003.
- [14] M. Aidelsburger, M. Atala, M. Lohse, J. T. Barreiro, B. Paredes, and I. Bloch. Realization of the hofstadter hamiltonian with ultracold atoms in optical lattices. *Phys. Rev. Lett.*, 111(18):185301–, October 2013.

- [15] Hirokazu Miyake, Georgios A. Siviloglou, Colin J. Kennedy, William Cody Burton, and Wolfgang Ketterle. Realizing the harper hamiltonian with laser-assisted tunneling in optical lattices. *Phys. Rev. Lett.*, 111:185302, Oct 2013.
- [16] Gregor Jotzu, Michael Messer, Remi Desbuquois, Martin Lebrat, Thomas Uehlinger, Daniel Greif, and Tilman Esslinger. Experimental realization of the topological haldane model with ultracold fermions. *Nature*, 515(7526):237–240, Nov 2014.
- [17] M Aidelsburger, M Lohse, C Schweizer, M Atala, J T Barreiro, S Nascimbène, N. R. Cooper, I. Bloch, and N. Goldman. Measuring the Chern number of Hofstadter bands with ultracold bosonic atoms. *Nature Physics*, 11(2):162–166, December 2014.
- [18] M. Mancini, G. Pagano, G. Cappellini, L. Livi, M. Rider, J. Catani, C. Sias, P. Zoller, M. Inguscio, M. Dalmonte, and L. Fallani. Observation of chiral edge states with neutral fermions in synthetic hall ribbons. *Science*, 349(6255):1510–, Sep 2015.
- [19] M Hafezi, S Mittal, J Fan, A Migdall, and J M Taylor. Imaging topological edge states in silicon photonics. *Nat. Photon.*, 7(12):1001–1005, October 2013.
- [20] A. Celi, P. Massignan, J. Ruseckas, N. Goldman, I.B. Spielman, G. Juzeliunas, and M. Lewenstein. Synthetic gauge fields in synthetic dimensions. *Phys. Rev. Lett.*, 112(4):043001–, Jan 2014.
- [21] B. K. Stuhl, H.-I. Lu, L. M. Ayccock, D. Genkina, and I. B. Spielman. Visualizing edge states with an atomic bose gas in the quantum hall regime. *Science*, 349(6255):1514–, Sep 2015.
- [22] Y. Aharonov and D. Bohm. Significance of electromagnetic potentials in quantum theory. *Phys. Rev.*, 115:485, 1959.

- [23] Yakir Aharonov and Ady Stern. Origin of the geometric forces accompanying berry's geometric potentials. *Phys. Rev. Lett.*, 69(25):3593–3597, 1992.